MulT_predict - An optimised comprehensive multicomponent geothermometer

Lars H. Ystroem, Fabian Nitschke, Thomas Kohl

Karlsruhe Institute of Technology (KIT), Campus South, Adenauerring 20b, 76131 Karlsruhe, Germany
Institute of Applied Geosciences (AGW), Professorship of Geothermal Energy and Reservoir
Technology

lars.ystroem@kit.edu, fabian.nitschke@kit.edu, thomas.kohl@kit.edu

**Abstract**

In this study, we introduce MulT_predict as a fully integrated solute multicomponent geothermometer, combining numerical optimisation processes for sensitive parameters to back-calculate to chemical reservoir conditions. This results in a state of the art geothermometer, providing an accurate reservoir temperature estimation validated by geothermal borehole measurements on a worldwide scale. In addition, a universally valid mineral assemblage for an unknown reservoir composition is developed, focusing on worldwide applicability. Using the evolved methodology, the limits of the optimisation processes are determined by using a synthetic brine (150°C, pH 6, aluminium concentration 0.003 mmol/l) and successively perturbing its geochemical equilibrium state. Individual back-calculation of reservoir conditions lead to valid temperature estimations of 145°C, 3.4% lower than the initial temperature while a simultaneous and interdependent optimisation reconstructs the sensitive parameters even more precisely with a deviation of 0.056 for the initial pH value, and 0.164 µmol/l for the aluminium concentration.

**Keywords**

MulT_predict, multicomponent geothermometry, reservoir temperature estimation, universally valid mineral set, benchmarking

## 1. Introduction

Evaluating the quantity of energy in a reservoir is essential for an economical geothermal energy production. Therefore, the accurate determination of the reservoir temperature is one key factor in geothermal exploration besides flow rate. Chemical geothermometry is a common technique to predict the reservoir temperatures from the geochemical composition of geothermal fluids. Temperature-dependent cation ratios, as well as the saturation state of mineral phases, can be the basis for temperature estimation, assuming an in-situ chemical equilibrium of the reservoir rock and fluid (Ellis and Mahon, 1964). As a result, the first conventional solute geothermometers were

introduced around 60 years ago by Fournier and Rowe (1966). In an ongoing development, new solute geothermometers were continuously developed but led to high uncertainties due to changes in fluid chemistry regarding different geothermal locations (Nitschke et al., 2018). Reed and Spycher (1984) plotted saturation indices of mineral phases calculated from thermodynamic data against temperature. The resulting saturation curves illustrate the temperature-dependent solubility of the reservoir mineral assemblage in the geothermal fluid. Spycher et al. (2014) took up this methodology and presented a multicomponent geothermometer, which evaluates the geochemical equilibria of mineral phases and fluid for reservoir temperature estimation. Nitschke et al. (2017) analysed temperature predictions from conventional and multicomponent geothermometers, showing a large reduction in uncertainties for this modelling approach. Thus, multiple mineral phases lead to statistically more robust temperature estimations. Therefore, Spycher et al. (2011) introduced the multicomponent geothermometer GeoT, followed by RTEst by Palmer (2014). Also, software for the chemical reconstruction of downhole and reservoir conditions like WATCH (Bjarnason, 2010) improved the results of solute geothermometry. GeoT uses Newton-Raphson iteration to calculate the geochemical equilibria of mineral phases from external thermodynamic databases (Sonnenthal et al., 2013). To compute temperature estimations, a complete fluid analysis is necessary. The program allows reconstructing the deep fluid composition (pH value, gas loss, dilution, and mixing) needing additional gas chemistry as well as end-member solutions. Recently, a python script was developed to search for the most suitable mineral assemblage for reservoir temperature estimation (Olguín-Martínez et al., 2022). RTEst uses the weighted sum of squares of the saturation indices of mineral phases to calculate the reservoir temperature estimation optimising the calculation by $CO_2$ fugacity and the mass of water (Palmer, 2014). Developing MulT_predict, Ystroem et al. (2020) combined the multicomponent temperature estimation with a numerical reconstruction of the reservoir conditions. The scope of MulT_preidct is to reconstruct the parameters, which control mineral solubility and are prone to secondary changes. Hence, sensitive parameters such as the aluminium concentration and pH value are back-calculated to reconstruct in-situ conditions (Ystroem et al., 2021). In addition, effects from secondary processes such as dilution and boiling are corrected. These parameters are prone to geochemical changes of the fluid during the ascent to the surface or while sampling (Giggenbach, 1981, 1988). The major advantage of MulT_predict, unlike other solute multicomponent geothermometers, is that a standard fluid analysis is sufficient and a sophisticated gas analysis is not required. In addition, all optimisation processes (pH value, aluminium concentration, boiling, and dilution) are calculated simultaneously and interdependently. Previously, MulT_predict was developed, applied, and validated for the basaltic setting of Krafla and Reykjanes fields in Iceland (Ystroem et al., 2020). The emphasis of this study is the development of a comprehensive multicomponent geothermometer for field exploration. At such an early stage, little reservoir knowledge and no borehole data is available. The

reservoir rock mineralogy as the basis of multicomponent geothermometrical temperature estimation is typically lacking. To facilitate the application of MulT_predict, as an early-stage exploration tool, for a broad range of geothermal sites, geological settings, and play types, the focus of the study is the development of a universally valid mineral set. Based on this, a general procedure of statistical outlier removal is introduced to acquire more precise temperature estimations and simplify the practicality of MulT_predict.

First, the applicability of the tool is transferred to a broad range of geothermal settings around the world including saline crystalline basements, marine, and continental basin facies as well as volcanic rock. In a first step, individual mineral sets are evolved for each geothermal setting. Afterwards, mineralogical coherences within the mineral sets are combined in a universally valid mineral set for general applicability. The subsequent outlier removal increases the precision of the temperature estimation. The results of the validation are shown for examples of boreholes. Furthermore, the characteristics of the site-specific brine are discussed to identify clustering and similarities concerning geochemical key parameters, providing insights into why a universally valid mineral set provides precise temperature predictions and where the limits of its application are. In the last part, MulT_predict's optimisation processes are benchmarked and discussed. Therefore, a predefined synthetic brine, initially in full equilibrium, is increasingly perturbed stepwise. This perturbation is then reconstructed using two different approaches. Firstly, each optimisation process is evaluated individually regarding the back-calculation of each sensitive parameter (boiling/dilution, pH value, and aluminium concentration). Secondly, the performance of the interdependent optimisation processes is evaluated by reconstructing all sensitive parameters together. Furthermore, the results of both reconstructions of reservoir conditions are discussed.

## 2. Methods

In solute multicomponent geothermometry, the base assumption is the geochemical equilibrium between the geothermal fluid and the hosted reservoir rock (Fournier and Truesdell, 1974). Thus, in the temperature-dependent reaction mineral phases are dissolved until an equilibrium within the fluid is reached. The geochemical equilibrium of each mineral phase is attained when the determined ion activity product *IAP* of the fluid equals the temperature-dependent thermodynamic constant *K(T)* (Equation 1). As a result, the temperature-dependent saturation index *SI(T)* of a mineral phase is zero.

$$SI(T) = \log \left( \frac{IAP}{K(T)} \right)$$

(1)

*SI* saturation index; *T* temperature; *IAP* ion activity product; *K* thermodynamic equilibrium constant

For reservoir temperature estimation, the saturation indices of several mineral phases are plotted against the temperature. The resulting equilibrium temperatures (at *SI* = 0) serve as a part of the geothermometer. Basing the temperature estimation on the *SI*s for several minerals has proven to be a robust geothermometric tool. As input parameters for MulT_predict, a standard geochemical fluid analysis covering the major cations and anions, the pH value, as well as silica and aluminium concentrations are needed to account for the chemical elements being the components of the reservoir rock mineral assemblage. Nevertheless, the geochemical equilibrium is still prone to uncertainties when the chemistry of the fluid changes. Divergences from the chemical equilibrium state are due to a) an immature fluid has not yet reached equilibrium or b) secondary processes while the fluid ascends to the surface or while sampling. Such processes refer to phase segregation, boiling, mixing, or dilution, as well as complex building and precipitation of mineral phases (Arnórsson et al., 1990) (Cooper et al., 2013) (Peiffer et al., 2014) (Spycher et al., 2014) (Nitschke, 2018). In a previous study, numerical optimisation processes are introduced to MulT_predict correcting sensitive parameters such as pH value, aluminium concentration, as well as changes in the fluid concentration from these effects (Ystroem et al., 2021). The goal is to reconstruct the in-situ chemical system as a basis to compute the equilibrium temperatures. Assuming that the temperature estimations for multiple mineral phases converge to an equal temperature. For these saturation index determinations, MulT_predict couples MATLAB to an IPhreeqcCOM server introduced by Charlton and Parkhurst (2011). The current IPhreeqc version (3.7.0 − 15749) is used to calculate the equilibrium state of a chosen mineral set to serve as a multicomponent geothermometer. Thermodynamic data for mineral phases are taken from our updated Lawrence Livermore National Laboratory (llnl.dat) database for high-temperature estimations (Ystroem et al., 2020). The major cation (Na, K, Ca, and Mg), and major anion (Cl, $SO_4$, $H_2S$, and $HCO_3$) as well as $SiO_2$, Fe, and Al concentrations are used as input data. In addition, to calculate the saturation indices of the mineral phases, the physicochemical parameters for the geothermal brine have to be defined. Therefore, the sampling pressure, temperature, as well as pH value are essential input data. MulT_predict distributes the input data to IPhreeqc to calculate the saturation indices *SI(T)* over a predefined temperature range *i* for previously selected mineral phases *j* (e.g. a universally valid mineral set). To identify the equilibrium temperatures for the mineral phases (*SI* = 0), the *SI(T)* returned from IPhreeqc are stored in a *i* x *j* matrix $A_{ij}$ and evaluated by the signum function in matrix $B_{ij}$ (Equation 2).

$$B_{ij} = \text{sign}(A_{ij}) := \lim_{k \to \infty} \frac{1 - 2^{-kA_{ij}}}{1 + 2^{-kA_{ij}}} = \begin{cases} -1 & \text{if } A_{ij} < 0 \\ 0 & \text{if } A_{ij} = 0 \\ 1 & \text{if } A_{ij} > 0 \end{cases} \tag{2}$$

Performing differences and approximate derivatives (Equation 3) upon the data returns the zero crossing of the saturation indices (Equation 1) of the chosen mineral set $j$ over their defined temperature range $i$, which are stored in a new matrix $C$.

$$C = \text{diff}\left(B_{ij}\right) = \begin{bmatrix} B(1,0) - B(0,0) & \cdots & B(1,j) - B(0,j) \\ \vdots & \ddots & \vdots \\ B(i,0) - B(i-1,0) & \cdots & B(i,j) - B(i-1,j) \end{bmatrix} \qquad (3)$$

To find the equilibrium temperature, the data of matrix $C$ are indexed by Equation 4 and transferred into an array $D$.

$$D = \text{for diff}\,(C) \neq 0 \qquad (4)$$

The resulting equilibrium temperatures $D$ and their mineral phases are both stored as cell entries in $E$. When the optimisation process is enabled, the selected sensitive parameters (boiling/dilution, pH value, and aluminium concentration) are iterated interdependently in their predefined range. After each computation, the result is also stored in the cell array $E$. Depending on the number of selected parameters $n$, the cell array $E$ is stocked up in $n$-dimensions. To get a consistent, statistically evaluable dataset, the mineral phases and their associated equilibrium temperatures are validated in each entry. Therefore, the cell entries of $E$ have to be cleaned up. An $n$-dimensional loop compares all resulting mineral phases and their temperatures from beginning to end. Missing temperature data is filled up with *NaN* while the names of $j$ are added as the associated phases. Simultaneously, redundant and excess information is removed. After the completion, the procedure is executed vice versa starting at the end to check for inconsistency within the updated array $E$. Then, the cell array $E$ is analysed by comparing the 0.25 and 0.75 quantiles, the interquartile range IQR, as well as the 1.5*IQR outliers within each entry stored in an array $F$ (Equation 5).

$$F_n = [(q_{0.75} + 1.5 * IQR) - (q_{0.25} - 1.5 * IQR)]; \text{ for all entries in } E \qquad (5)$$

Afterwards, MulT_predict statistically evaluates all $n$-dimensional cell entries of $F_n$ for the minimum element of the array excluding *NaN* values. The global minimum represents the maximal convergence of the equilibrium temperatures of the considered mineral phases (Equation 6).

$$\min\left(f(x_0)\right), \ F_n \subseteq \mathbb{R}^+, \ x_0 \in F_n, \ f: F_n \to \mathbb{R}^+, \text{ if } (\forall x \in F_n)\, f(x_0) \leq f(x) \qquad (6)$$

Determining the position of the global minima in the array $F_n$, the back-calculated in-situ values of the reservoir parameters are extracted. In the last step, MulT_predict re-evaluates the in-situ reservoir parameters and re-calculates the final temperature estimation. The final results are output graphically and tabular.

## 3. Data & Results

To develop a comprehensive multicomponent geothermometer and a universally valid mineral assemblage MulT_predict has to be validated for a variety of geothermal sites. A thorough validation is only possible with datasets, where geochemical fluid analyses, as well as borehole temperatures, are available. Geothermal sites were intentionally selected in a way, that the data covers a broad range of different lithologies, temperatures, and geochemical characteristics to evolve a comprehensive tool. The geothermal fluid samples from different geothermal sites are mostly compiled from the literature. In sum, eight geothermal settings were evaluated (Table 1). To validate MulT_predict, geochemical data, as well as in-situ reservoir temperature measurements of the reservoir, must be available for each site. The sites are categorised by their geology and tectonic setting: crystalline basement of a rift basin, sedimentary back-arc basin dominated by continental facies, foreland basin dominated by marine facies, sedimentary basin dominated by marine facies, volcanic facies dominated by andesite to rhyolite at subduction zones, and basaltic facies on the mid-ocean ridge induced by a hotspot.

*Table 1: Collocation of the lithology, geological setting, location, and references of the geothermal wells for the validation of MulT_predict.*

| Lithology | Setting | Location | Reference |
|---|---|---|---|
| Granite | Basement (rift basin) | Upper Rhine Graben | Sanjuan et al. (2001) |
| | | | Schindler et al. (2010) |
| | | | Dezayes et al. (2013) |
| | | | Sanjuan et al. (2016) |
| | | | Vidal and Genter (2018) |
| | | | Vidal et al. (2019) |
| Lacustrine facies | Back-arc basin | Pannonian Basin | Varsányi et al. (1997) |
| Marine facies, Malm | Foreland basin | German Molasse Basin | Internal communication |
| Marine facies, Dogger | Sedimentary basin | Paris Basin | Michard and Bastide (1988) |
| | | | Marty et al. (1988) |
| | | | Criaud et al. (1989) |
| Rhyolite, Andesite | Subduction zone | Waiotapu | Banwell (1959) |
| | | | Ellis and Mahon (1977) |
| | | | Giggenbach et al. (1994) |
| Andesite | Subduction zone | Miravalles | Dennis et al. (1989) |
| | | | Gherardi et al. (2002) |
| Dacite | Subduction zone | El Tatio | Ellis and Mahon (1977) |
| | | | Giggenbach (1978) |
| Basalt, hyaloclastite | Hotspot | Iceland | Guðmundsson and Arnórsson (2002) |
| | | | Óskarsson et al. (2015) |

The data representing the highly saline fluid of sedimentary origin hosted in the granitic crystalline basement in the Upper Rhine Graben (URG) is presented by Sanjuan et al. (2001) and Schindler et al. (2010) for GPK 1 and 2 in Soultz-sous-Forêts, Dezayes et al. (2013) and Vidal et al. (2019) for GRT-1 in Rittershoffen, and Sanjuan et al. (2016) as well as Vidal and Genter (2018) for GTLA-1 in Landau and INSH in Insheim. The continental sedimentary facies is represented by lacustrine to fluvial sedimentary sequences in the Pannonian Basin published by Varsányi et al. (1997). Malm layers in the German Molasse Basin represent marine facies in a foreland basin (internal communication with power plant operators, Appendix A). Marine sedimentary facies from Dogger layers in the Paris Basin were published by Michard and Bastide (1988), Marty et al. (1988), and Criaud et al. (1989). The volcanic facies are summing up different types of reservoir rock around the Pacific Ring of Fire. For Waiotapu in New Zealand, rhyolite and andesite reservoir formations are hosting the geothermal wells published by Banwell (1959), Ellis and Mahon (1977), and Giggenbach et al. (1994). Further, data from the wells of the andesite reservoir formation in Miravalles, Costa Rica, are presented by Dennis et al. (1989), and Gherardi et al. (2002). Lastly, the geochemical data presented by Ellis and Mahon (1977), and Giggenbach (1978) of a dacite reservoir in an ignimbrite formation at El Tatio, Chile, are used. The basalt and hyaloclastite facies are visualised by data from Krafla (Guðmundsson and Arnórsson, 2002), and Reykjanes (Óskarsson et al., 2015). For reference, the artificial standard of ocean water is illustrated (ASTM D1141-98, 2013).

To establish the new procedure for unknown temperature estimations three steps had to be passed. First, setting-specific mineral sets were developed for known mineralogical and temperature data. Second, coinciding mineral phases of setting-specific mineral sets are combined into a universally valid set. Third, to refine the general temperature estimation, a procedure of outliner removal has to be implemented. The results of the three steps are visualised in Figure 1.

For each geothermal setting, the mineral set for reservoir temperature estimation is compiled individually (Appendix B). Creating these unique sets is time-consuming. Therefore, if known, the observed mineral composition of the reservoir rock should be transferred into a mineral set. Hence, the main mineral phases of the reservoir rock, as well as secondary and accessory minerals, have to be considered. The resulting mineral assemblages have to be refined until the optimised saturation curves converge on each other, minimising the uncertainty of the temperature estimation (c.f. Equation 5, 6). Therefore, mineralogical foreknowledge of the reservoir rock composition and its secondary mineralisation is preferable in general. Nevertheless, in some cases this information is not available or unknown, thus, a predefined universal mineral set is presented. This universally valid mineral set consists of the most common rock-forming minerals as well as secondary and accessory minerals. The focus of the universal set is its comprehensive applicability while providing still reasonable temperature estimations. Together with the upcoming procedure of outlier removal, the temperature

estimations get more precise. Thus, all evolved setting-specific mineral sets were compared among themselves. As a result, in most of the sets, an overlap of mineral phases is repeatedly equilibrated. Combining them, a universally valid mineral set has been established, which can be applied on a worldwide scale independently of reservoir mineralogy and setting. This universally valid set consists of quartz, K-feldspar, microcline, albite, muscovite, illite, diaspore, analcime, scolecite, anhydrite, kaolinite, and pyrophyllite (Appendix B). Figure 1 illustrates the outlier removal procedure to obtain the most reasonable temperature estimation. In the diagram, three temperature estimations per geothermal setting are shown. The orange box indicates the measured in-situ temperature corresponding to the open hole section within the example. The first boxplot (magenta) illustrates the temperature estimation by just applying the universally valid mineral set. In the next step, for the second boxplot in green, two statistical outliers of the universal set are removed. This corresponds to mineral phases $M$, which are exceeding 1.5 times the interquartile range (IQR) the most (Equation 7).

$$M \subseteq \mathbb{R}^+, y \in M, \begin{cases} \text{if } y > y_{median} + 1.5 * IQR \\ \text{if } y < y_{median} - 1.5 * IQR \end{cases} \tag{7}$$

This outlier removal represents the procedure, which is used to evaluate new geochemical data with unknown mineralogy. The third boxplot in blue visualises the best fitting result obtained by developing an individual mineral set for each setting, as mentioned in Appendix B. After the universally valid mineral set for reservoir temperature estimation has been introduced, it can be compared to the results of the outlier removal and each setting-specific mineral set (Appendix B). Comparing the three boxplots in Figure 1, the shift of temperature estimation towards the measured in-situ temperature is evident. In each case, the overall spread of the plot is decreasing as well as a decreasing or steady IQR. Only for the carbonate facies of the Paris Basin and the Molasse Basin, calcite and dolomite have to be added to the universally valid mineral set to reconstruct reservoir conditions and temperature estimations more precisely.
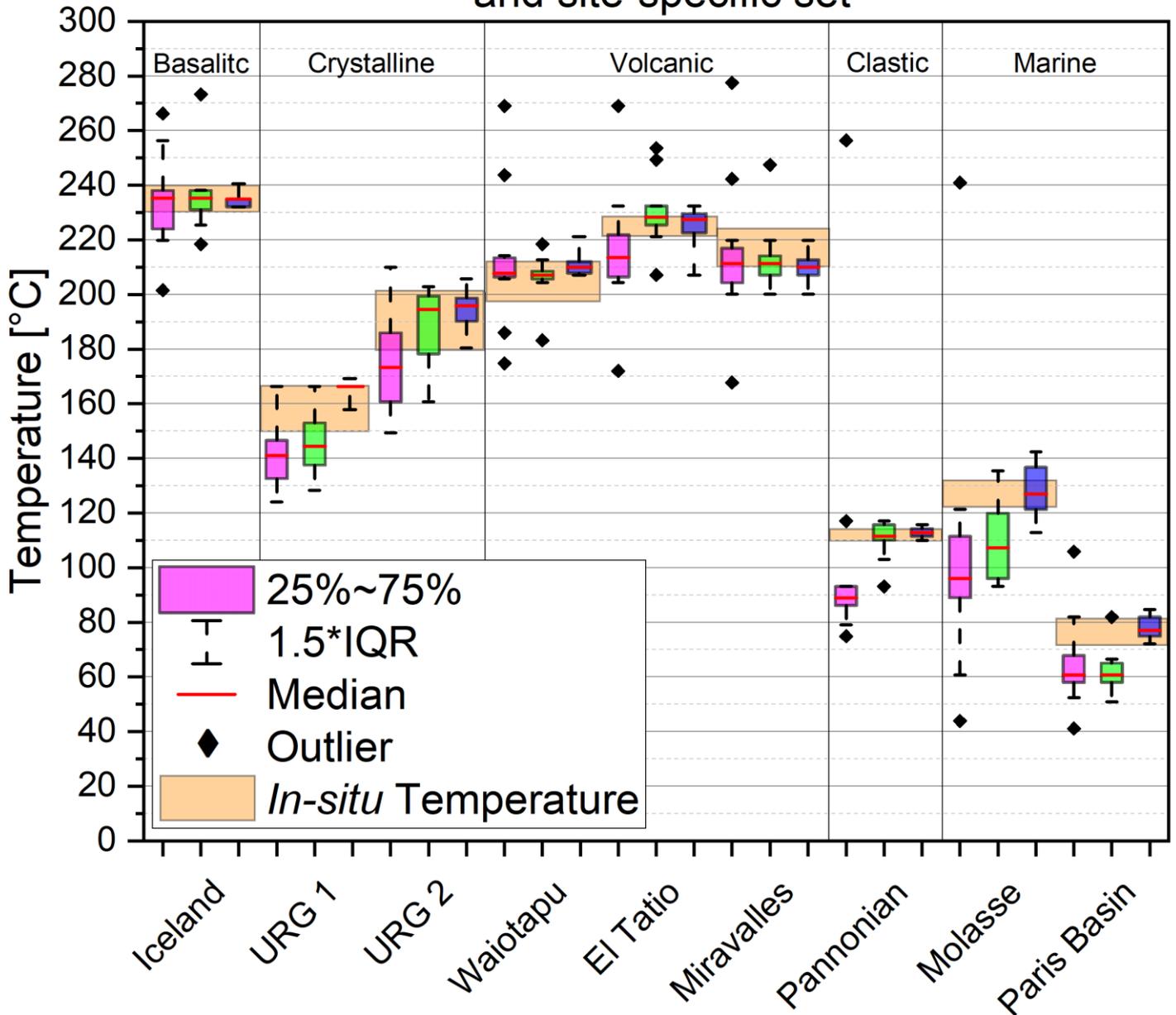
Figure 1: Comparison of three temperature estimations for an exemplary well of individual geothermal settings around the world (Krafla on Iceland, Soultz-sous-Forêts in the Upper Rhine Graben, Waiotapu in New Zealand, El Tatio in Chile, Miravalles in Costa Rica, Makó in the Pannonian Basin, Unterhaching in the German Molasse Basin, and Evry in the Paris Basin). Straight lines separate different reservoir rock compositions (basaltic, crystalline, volcanic, clastic, and marine facies). The orange box indicates the measured in-situ temperature in the open hole section of the well. The first boxplot (magenta). visualises the temperature estimation with the original universally valid set The secondary boxplot is obtained by reducing the outermost mineral phases (black diamonds) within the universal set and recalculating the temperature estimation (outlier reduction in green). In comparison, the third boxplot (blue) is the best-fitting mineral set individually developed for each setting (cf. Appendix B).

For Iceland, the outlier removal reduces the IQR by 50 % to 7 K, while the median temperature remains at 235°C, fitting the best-fit temperature and the temperature log. For URG, two samples of GPK2 in Soultz-sous-Forêts are presented. URG 1 was sampled in the year 1997 when the well reached 3876 m depth. URG 2 was sampled in the year 1999 after deepening the well down to 5093 m representing the actual temperature at the bottom of GPK2. For URG 1, the overall uncertainty decreases by 12%

due to the outlier removal, but further refinement of the mineral set is necessary to reach best-fit conditions at 166°C. For URG 2, the outlier removal decreases the spread of the boxplot by 18 K. The best-fit temperature estimation matches the measured in-situ temperature of the open hole section. The two temperature estimations of GPK2 illustrate the importance of the equilibrium reaction between the hosted reservoir and the fluid, where the technical available temperatures are predicted. At Waiotapu, the necessity of outlier removal for the magenta boxplot is clear. The removal reduces the spread by 59 K and emphasises the median temperature at 207°C within the measured temperature. In addition, the IQR (4 K) of the adjusted universally valid mineral set equals the best-fitting result. For El Tatio, the overall spread is reduced by 50% due to the outliner removal and increases the median temperature to its final result at 228 °C, matching the measured in-situ temperature. The outlier removal for Miravalles diminishes the spread by 62 K and the IQR by 45%. Likewise, the adjusted universally valid mineral set resembles the best-fitting plot. For the Pannonian Basin, the procedure shifts the median temperature by 22 K into the measured temperature range. Compared to the best-fitting plot, the mineral assemblage can be further refined to increase accuracy. For both marine facies, the outlier removal reduces the uncertainties but the temperature estimation does not fit the in-situ temperature. For the Molasse Basin, the spread diminishes by 79%, while for the Paris Basin its halves. Due to the lack of carbonate mineral phases within the universally valid mineral set, the median of the temperature estimation in the Molasse is 20 K beneath the best fit and in the case of Paris Basin 16 K.

4. **Discussion**

For the illustration of coherence of the properties of brines from different geothermal settings, geochemical key parameters are analysed. These parameters are relevant to multicomponent geothermometry and can explain the plausibility of a generally valid mineral set. For this purpose, the major chemical components are used (Na, K, Ca, Mg, Cl, $SO_4$, $HCO_3$, and additionally pH). To graphically cluster the brines according to the surrounding lithology, strongly temperature-sensitive components such as $SiO_2$ were omitted. Thus, the major chemical components of dissolved mineral phases used in geothermometry are evaluated. Thus, the graphical single-point method by Langelier and Ludwig (1942) is modified. In the original two-dimensional plot, the pH value of the fluid is added as the z-axis. Furthermore, the total dissolved solids TDS are projected as sphere size $s$ (Equation 8).

$$s = \log{(TDS * 10)} \tag{8}$$

To display the differences in sphere sizes homogenously, the TDS is multiplied by ten and then the decadic logarithm is applied. Hence, standard fluid analysis of the geothermal brines are plotted in the modified Langelier-Ludwig diagram (Figure 2).
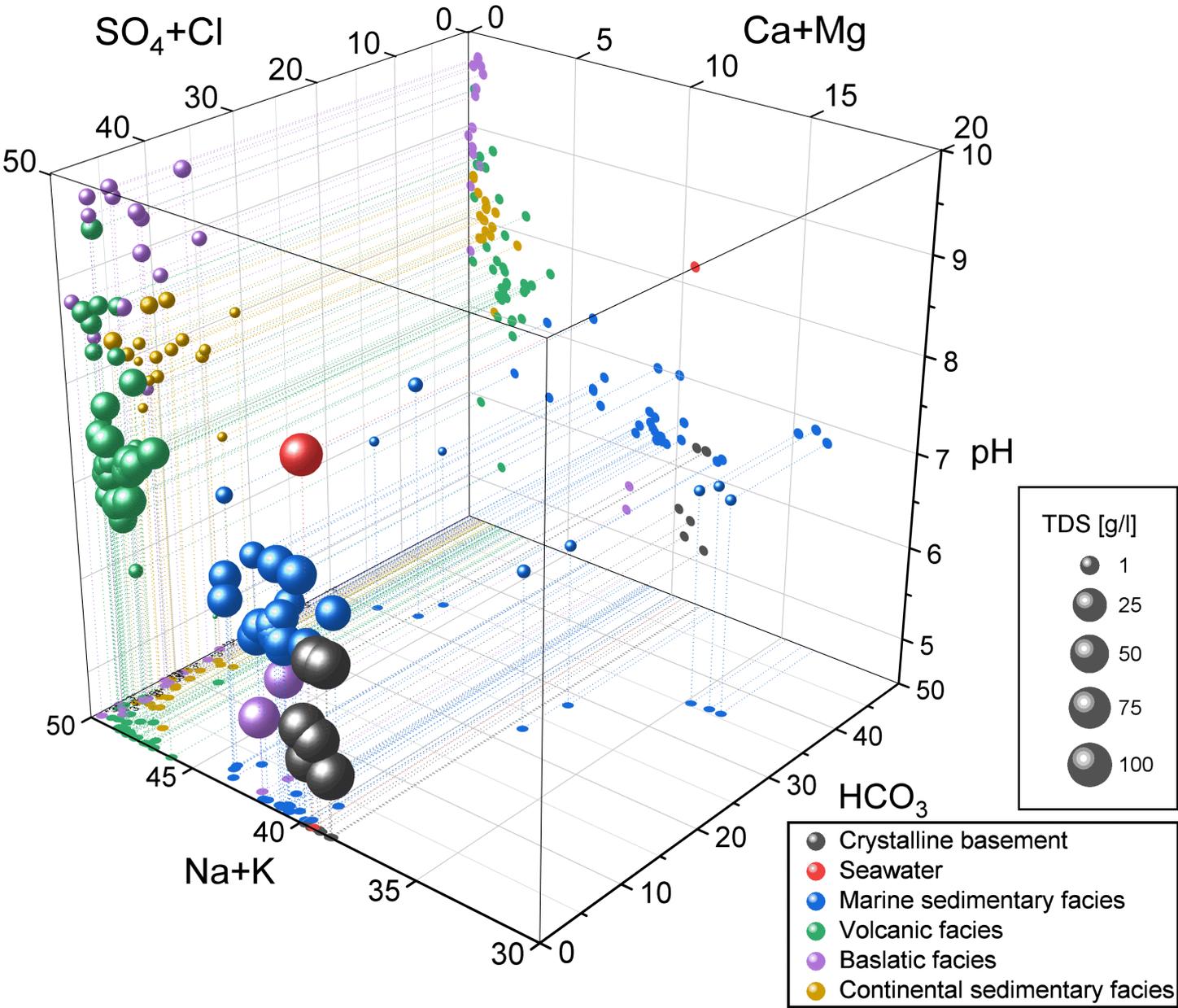


*Figure 2: Modified Langelier-Ludwig diagram for classification of geothermal settings in different facies. The pH value was added as a third dimension (z-axis) as well as the total dissolved solids (TDS) visualised in sphere size.*

By plotting the geochemistry of the different geothermal sites clustering can be observed. High saline brines from the Dogger formation in the Paris Basin, the saltwater intrusion in the wells of the Reykjanes Peninsula, as well as the samples from the Upper Rhine Graben, cluster below the salinity of seawater at Na+K 40% and SO$_4$+Cl 50%. The shift in pH value is a function of temperature and salinity (Ellis, 1970). Increasing temperature and salinity cause the pH value to decrease. The marine facies samples cluster near-neutral pH values. This corresponds to a buffering reaction within the carbonates

(Malm, Dogger) due to calcite solubility equilibrium and temperature-dependent auto-dissociation within the fluid (Ellis, 1963). Therefore, the brines in the URG (TDS ~ 100 g/L) and high-temperature settings in Reykjanes (exceeding 300°C) have lower pH values. For the volcanic facies, Miravalles and El Tatio are forming the main cluster around Na+K 47% and $SO_4$+Cl 50% with a pH of 7.5. The samples of Waiotapu have a shift to higher pH values. For Waiotapu, Giggenbach et al. (1994) proposed a low content of $CO_2$ within the parent magma and removal of $CO_2$ as calcite through Ca-Al-silica interaction. In addition, there is degassing and dilution of the fluid before reaching the wells. The well waters in Krafla and Námafjall cluster at the highest pH values. These waters are low mineralised and of meteoric origin. Due to degassing of $CO_2$ and $H_2S$ the pH is increased as well as a bicarbonate concentration trend up to 15% of $HCO_3$ corresponding to an increase in magmatic activity underneath well K-20 (Guðmundsson and Arnórsson, 2002). For samples from the Pannonian Basin, the TDS concentration is low. The fluid chemistry clusters next to Waiotapu samples. Similar to the bicarbonate trend in Icelandic samples, the Pannonian chemistry shows the $HCO_3$ concentration increasing with temperature and depth corresponding to lacustrine carbonates within the formations (Varsányi et al., 1997).

The clustering of samples in the Langelier-Ludwig diagram (Figure 2) shows up similarities within the unique signature of each geothermal setting. In addition, the influence of evaporites and seawater can clearly be distinguished from samples of meteoric origin. The distribution of pH values represents a variety of geochemical processes coupled to the individual settings. The pH value sums up buffer reactions, degassing processes, and the impact of salinity and temperature. Therefore, the geochemistry of the geothermal fluid is an indicator of the mineral composition leached out of the reservoir rock. Thus, these similarities in the clustering are reflected in the universally valid mineral assemblage presented for reservoir temperature estimations.

Furthermore, the optimisation process within MulT_predict is evaluated. Therefore, a synthetic brine is set up and processed by MulT_predict to back-calculate the initial brine temperature. In the next step, all parameters of the optimisation processes are tested individually. In this case, the influence of salinity, steam loss, and dilution, the pH value as well as the Al concentration are examined. Therefore, the synthetic brine is increasingly perturbed stepwise for one of these parameters at once. This is resumed until the numerical limits of the optimisation of MulT_predict are reached. Thus, the individual optimisation processes can be evaluated. Lastly, the synthetic brine is perturbed for all parameters at once. The steam loss and dilution are increased stepwise, while random pH values and element concentrations in a predefined range are added. In this case, the MulT_predict's optimisation process is used interdependently to back-calculate reservoir conditions.

The synthetic mineral assemblage is equilibrated at 150°C and has a pH value of six. The mineral assemblage is composed of phases of the universally valid set: quartz, microcline, albite, calcite,

anhydrite, muscovite, illite, and stilbite. The resulting equilibrated fluid lost some mass while reacting with stilbite (0.899 kg remaining) as well as the pH value increased to 6.743 due to changes in the activity of hydrogen ions. To revert to initial conditions, the fluid mass is set back to 1 kg. In the next step, each parameter is varied individually and stepwise around its initial value to perturb the equilibrium between mineral phases. Then, MulT_predict's optimisation process is used to reconstruct the equilibrium conditions of the fluid and determine the initial equilibrium temperature. First, the salinity is increased in 100 steps from zero molar up to five molar by adding NaCl to the solution. In Figure 3, for each increment, the MulT_predict computes the temperature estimations which are plotted in the diagram. The computed temperature estimation is constantly at 148°C close to the initial conditions of 150°C, thus MulT_predict temperature estimations show virtually no sensitivity to increasing salinity.
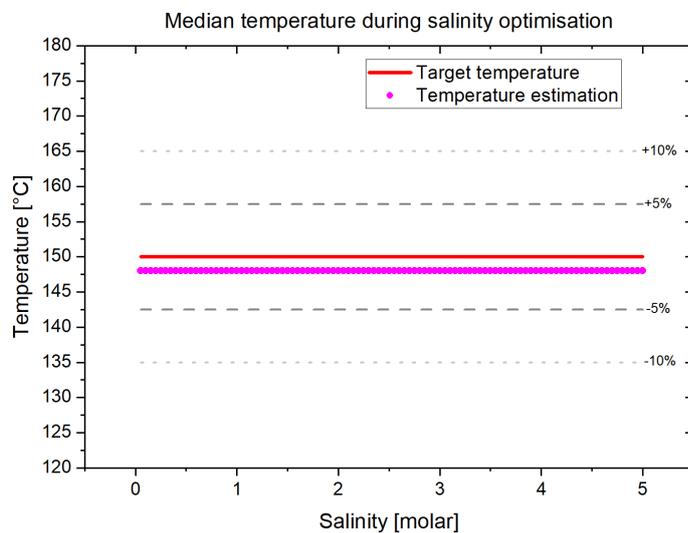


Figure 3: Temperature estimations corresponding to salinity changes from zero to five molar by adding Na Cl to the solution. The red line is indicating the initial equilibrium temperature of the synthetic fluid. The red line indicates the equilibrium temperature of 150°C.

The assessment of the sensitivity of changes by steam loss and dilution in the fluid is displayed in Figure 4. Therefore, the moles of the fluid are altered by 1% per step. For dilution, 0.555 moles of pure water are added per increment. In contrast, 0.555 moles of pure water are subtracted mimicking steam loss. In MulT_predict's optimisation process, these changes are back-calculated. On the left side a) of Figure 4, MulT_predict's computed concentration error is plotted against the percentage of changes to the fluid concentration as well as the resulting temperature estimation on the right side b).
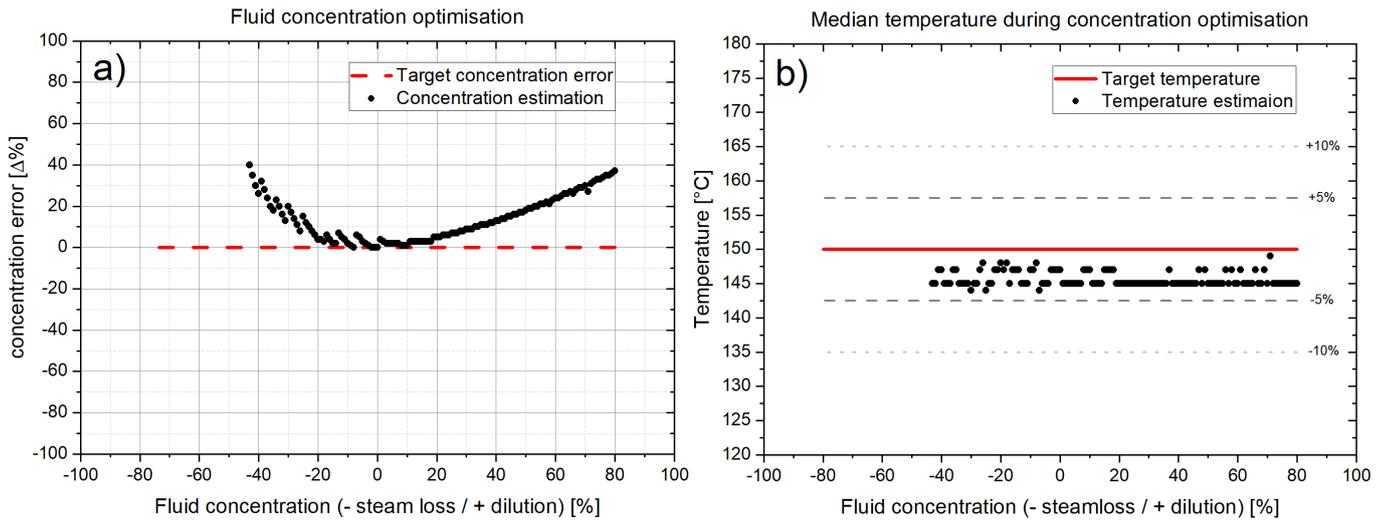
*Figure 4: On the left side a), the error of the reconstructed fluid concentration is plotted against the changes to the mass of water within the fluid. The dashed red line indicates the targeted error. In the right graph b), the corresponding temperature estimations are visualised, while the solid red line indicates the targeted temperature of 150°C.*

For perturbations within ±20% of dilution or steam loss, the optimisation process reconstructs the fluid with small errors of 3 percentage points on average (cf. dashed, red line in Figure 4). Regardless of whether steam loss or dilution, at higher changes MulT_predict starts to underestimate these perturbations. Thus, the difference between the synthetic changes in the fluid and the reconstruction is rising. This curve shape corresponds to the geochemistry in the fluid. Decreasing water by 50% doubles the element concentration. In contrast, dilution of 100% halves the concentration. Comparing the resulting element concentration leads to a continuous increase in error. Nevertheless, the temperature estimations on the right side of Figure 4 have a maximum spread of five Kelvin (144°C to 149°C) and are on average 145°C. The red line indicates the equilibrium temperature of the synthetic set.

Furthermore, changes in the pH value are evaluated in Figure 5. The pH value varies between five and seven in 200 increments. The resulting pH value of the optimisation process is plotted in a) against the synthetic pH variation. In b), the resulting pH value is illustrated against the temperature estimation.
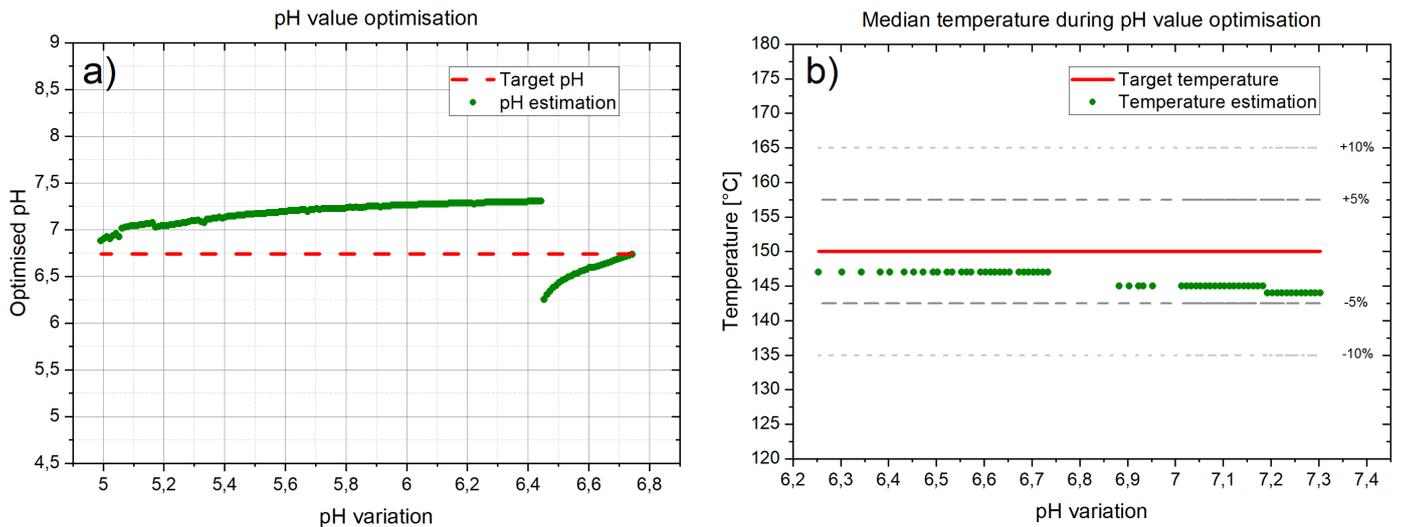
*Figure 5: On the left side a), the reconstructed pH value of the fluid is plotted against its variation between five and seven. The dashed red line indicates the initial equilibrium pH at 6.743. In the right graph b), the corresponding temperature estimations are visualised, while the solid red line indicates the targeted temperature of 150°C.*

Figure 5 a) visualises the difference between the resulting optimised pH value and the initial equilibrate pH (6.743) indicated by the dashed, red line. pH values increasing 6.743 cannot be back-calculated by IPhreeqc because of a thermodynamic equilibrium gap for the aluminium concentration at higher pH. Therefore, MulT_predict is also capped at this level, not allowing interdependent optimisation yet. The estimations of the pH value show a pattern corresponding to geochemical adaptations of IPhreeqc iteration steps. Because of the loss in precision due to no redox buffering, IPhreeqc alters parameters automatically. Therefore, the redox potential is varied so the balance equations can be solved to obtain a chemical equilibrium (Parkhurst and Appelo, 2013). This leads to a recommencement at pH 6.443 and a steady decline in the optimised pH value towards the initial value while the redox potential is adjusted. In Figure 5 b), optimised pH values in the range 7.303 to 7.193 reach a temperature estimation of 144°C. For values from 7.183 to 6.883 the estimation is 145°C and for a lower pH, a temperature of 147°C is calculated.

Finally, variations in the aluminium concentration are examined. In 160 steps, 80% of the initial

aluminium concentration is added and subtracted. Figure 6 illustrates the optimised aluminium concentration against the shift in concertation as well as the resulting temperature estimation.
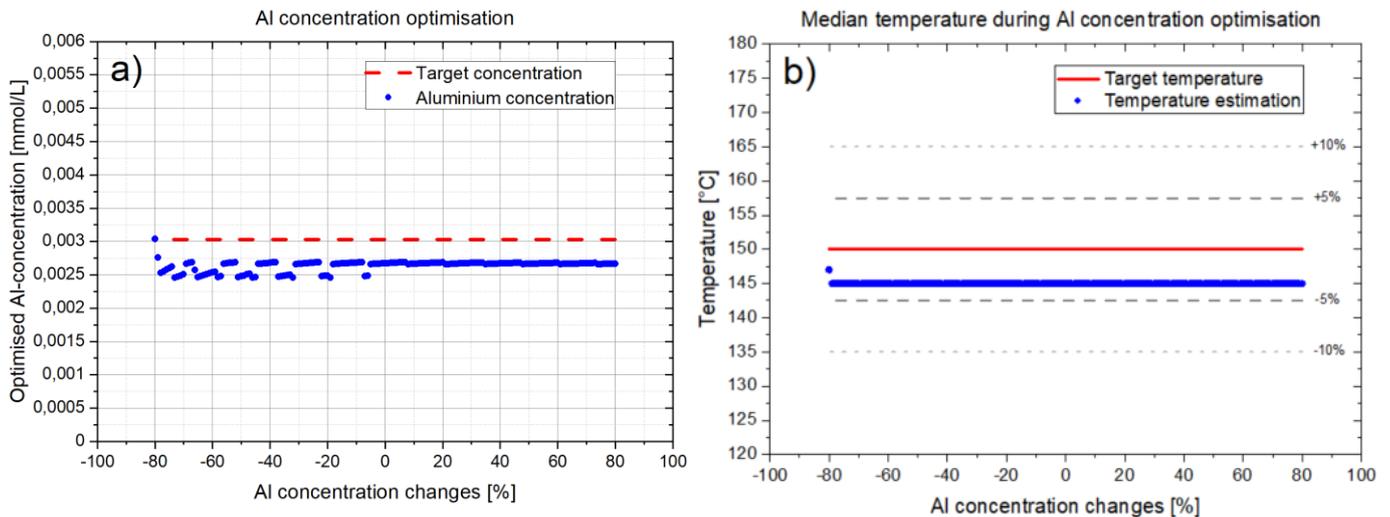


*Figure 6: On the left side a), the reconstructed aluminium concentration is plotted against its variation between -80% and +80%.The dashed red line indicates the initial aluminium concentration of 0.00303 mmol/l. In the right graph b), the corresponding temperature estimations are visualised, while the solid red line indicates the targeted temperature of 150°C.*

Figure 6 a) shows a steady back-calculated aluminium concentration around 0.00267 mmol/l (11% less than the initial 0.00303 mmol/l) for raising concentrations. With decreasing aluminium concentration, IPhreeqc starts to iterate the equilibrium calculation to converge the chemistry. Due to the variation in the overall small aluminium concentration, errors accumulate while running the simulation. Thus, the program automatically attempts to solve the calculation by altering and combining tolerances and step sizes to fit the solution (Parkhurst and Appelo, 2013). Similarly, the redox potential is adjusted. Therefore, the aluminium concentration fluctuates from 0.00245 mmol/l to 0.00269 mmol/l and reaches the maximum of 0.00304 mmol/l at -80%. However, the temperature estimation is steady at 145°C once rising to 147°C at -80%.

Comprising all cases, MulT_predict underestimates the temperature estimations, anyhow not exceeding 6 K (4% error). Only optimising individual parameters does not take chemical interactions into account. As mentioned in the methodology, these sensitive parameters are coupled due to secondary processes. Therefore, in a second step, the back-calculation process is tested by optimising the parameters interdependently. Therefore, in 5%-steps the fluid concentration was perturbed again between -45 % to 70%, as well as the values for the pH and Al concentration have been randomised. For the pH, random values between pH 5 and 7 and for the aluminium concentration values between 0.001 mmol/l and 0.006 mmol/l were generated. Currently, MulT_predict is allowed to simultaneously optimise all sensitive parameters interdependently.
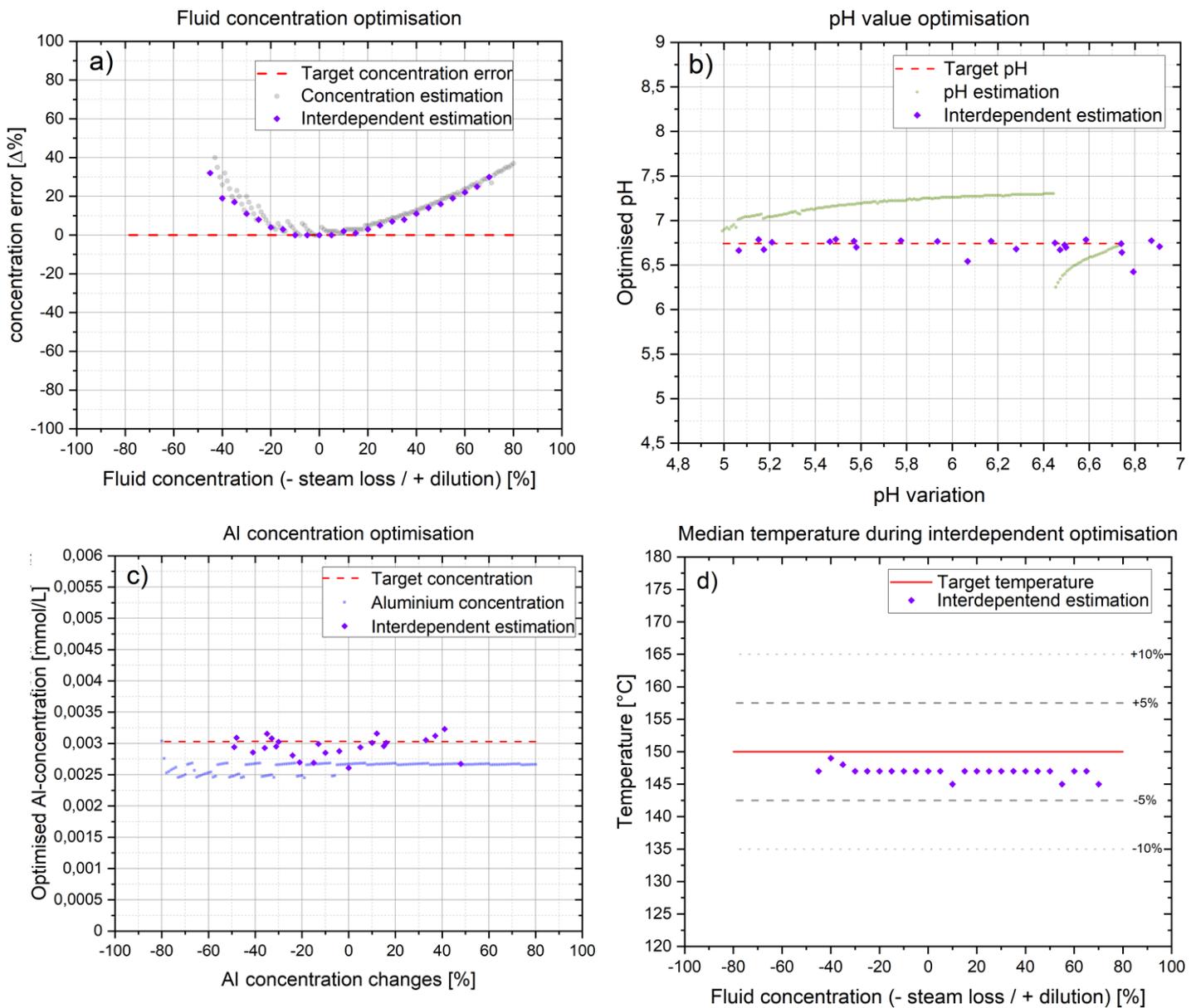
*Figure 7: Simultaneous and interdependent optimisation (purple) of all sensitive parameters plotted into each optimisation process (pale colours). a) shows the reconstructed fluid concentration resulting from the variation of the mass of water within the fluid. b) visualises the back-calculated pH value against its change. In c), the interdependent reconstruction of the aluminium concentration is plotted against its variation. d) illustrates the temperature estimation of the overall optimisation process. The dashed red lines indicate the initial equilibrium conditions, as well as the solid red line which shows the equilibrium temperature of the synthetic fluid.*

In Figure 7, the fluid concentration, pH value, and aluminium concentration are optimised simultaneously. The interdependent estimations from test step 1 were plotted into the results of the individual optimisation processes, which were paled out. In a), the average concentration error decreases by 2 percentage points compared to the result of the independent back-calculation. The pH values in b) and the aluminium concentrations in c) fit the target values more accurately than those resulting from the individual optimisation process. For the pH value, the maximum deviation is 0.3 less than the targeted pH. On average, the variance of the interdependent pH optimisation is 0.056, which is negligible compared to the mean deviation of 0.32 for the independent calculation. For the

aluminium concentration, the average deviation is 0.164 µmol/L about 5% of the target concentration. Therefore, interdependent optimisation is circa 50% more precise than independent optimisation. In addition, the temperature estimations in d) improved to a mean value of 147°C. Especially the reconstruction of the pH value and the aluminium concentration show the importance of an interdependent optimisation process to reflect geochemical changes within the fluid.

## 5. Conclusions

MulT_predict is a robust multicomponent geothermometer with a built-in optimisation process to reconstruct the initial in-situ reservoir conditions and temperature from a chemically perturbed geothermal fluid sample. The temperature estimations are based on a standard chemical analysis of the geothermal fluid composition. No sophisticated sampling methods nor analyses are needed. A numerical reconstruction process of the in-situ chemical conditions is implemented to correct secondary perturbation of the fluid sample. The joint optimisation of coupled key parameters (boiling/dilution, pH value, and aluminium concentration) allows for the determination of precise reservoir temperatures. A universally valid mineral set is deduced, allowing the calculation of reservoir temperatures. Regardless of the setting and the reservoir mineralogy, the universally valid mineral set provides a great advantage when only little or no knowledge of the subsurface mineralogy is available. The implementation of a statistical outlier removal refines the mineral assemblage and improves the temperature estimation further. Therefore, MulT_predict can be used as an early phase greenfield exploration tool, which has been validated at multiple geothermal sites worldwide.

The emphasis of the study was the enhancement of the applicability of MulT_predict on a worldwide scale, as well as the focus on the performance of the optimisation processes and their validation. The newly developed universally valid mineral set allows a first temperature estimation for geothermal systems of an unknown subsurface. The set contains twelve mineral phases (quartz, K-feldspar, microcline, albite, muscovite, illite, diaspore, analcime, scolecite, anhydrite, kaolinite, and pyrophyllite). These mineral phases are selected according to their common existence in geothermal systems worldwide causing similar chemical signatures (in terms of key parameters for multicomponent geothermometry) to fluids of very different settings. They consist of key mineral phases of major rock types, accessory minerals, secondary mineral phases, as well as polymorphic mineral phases. The developed universally valid mineral set is tested and validated at eight different geothermal sites (Iceland, Upper Rhine Graben, German Molasse Basin, Paris Basin, Pannonian Basin, Waiotapu, Miravalles, and El Tatio). This mineral set combines mineral phases of the associated geology of the settings (basaltic, volcanic, marine, and continental facies as well as crystalline basement).

The functionality of the optimisation processes is tested by perturbing an equilibrated synthetic mineral assemblage. Thus, four critical parameters are investigated: the salinity of the fluid, changes in the mass of water (steam loss and dilution), as well as variations in the pH value, and the aluminium concentration. First, each optimisation process is performed individually. Perturbation of the salinity does not affect the temperature estimation of MulT_predict. Perturbations in the mass of water, the pH value, and aluminium concentration lead to an average temperature estimation of 145°C and therefore, a reasonable error of 3.4%. For the interdependent optimisation process, the back-calculations for pH value and aluminium concentration resemble the initial conditions. The average temperature estimation is 147°C, 3 K less than the initial equilibrium temperature of 150°C. Considering all cases, MulT_predict and its built-in optimisation processes provide precise temperature estimations. Thereby, the interdependent optimisation process can back-calculate reservoir conditions more accurately than an individual parameter optimisation. However, the calculation of the interdependent optimisation process is more computation-intensive. Therefore, the number of coupled sensitive parameters should be optimised jointly. Overall, the introduced universally valid mineral set expands the usability of MulT_predict and its applicability for the user. In addition, the effectiveness of interdependent optimisation processes is verified, resulting in improved temperature estimations. Eventually, MulT_predict is a fully integrated comprehensive multicomponent geothermometer.

## 6. Data Availability

**Upper Rhine Graben**: Sanjuan et al. (2001); Schindler et al. (2010); Dezayes et al. (2013), Sanjuan et al. (2016); Vidal and Genter (2018); Vidal et al. (2019). **Pannonian Basin**: Varsányi et al. (1997). **German Molasse Basin**: c.f. Appendix A. **Paris Basin**: Michard and Bastide (1988); Marty et al. (1988); Criaud et al. (1989). **Waiotapu**: Banwell (1959); Ellis and Mahon (1977), Giggenbach et al. (1994). **Miravalles**: Dennis et al. (1989); Gherardi et al. (2002). **El Tatio**: Ellis and Mahon (1977), Giggenbach (1978). **Iceland**: Guðmundsson and Arnórsson (2002), Óskarsson et al. (2015).

## 7. Appendices

*Appendix A: Anonymised data from power plant operators from the German Molasse Basin. Element concentrations are presented in mg/l.*

| pH | Sampling temperature [°C] | $SiO_2$ [mg/l] | Na [mg/l] | K [mg/l] | Ca [mg/l] | Mg [mg/l] | Cl [mg/l] | $SO_4$ [mg/l] | $H_2S$ [mg/l] | $HCO_3$ [mg/l] | Fe [mg/l] | Al [mg/l] |
|---|---|---|---|---|---|---|---|---|---|---|---|---|
| 7.1 | 46.5 | 54 | 284 | 15.5 | 14.0 | 4.4 | 172.0 | 0.5 | 1.0 | 509.0 | 0.02 | 0.0870 |
| 7.3 | 34.9 | 20 | 353 | 13.2 | 30.7 | 7.3 | 400.9 | 0.0 | 0.2 | 390.4 | 0.16 | 0.0072 |
| 6.9 | 49.2 | 40 | 104 | 12.3 | 28.4 | 10.1 | 70.0 | 0.5 | 4.5 | 314.0 | 0.11 | - |
| 6.8 | 38.1 | 44 | 105 | 12.2 | 27.5 | 9.1 | 68.9 | 1.4 | 5.6 | 308.5 | 0.03 | 0.0060 |
| 6.2 | 41.3 | 103 | 162 | 30.5 | 38.9 | 5.7 | 169.0 | 35.0 | 11.3 | 289.2 | 0.09 | - |
| 6.4 | 24.8 | 130 | 111 | 16.3 | 3.2 | 1.1 | 68.3 | 16.3 | 6.5 | 192.8 | 0.03 | 0.0150 |

Appendix B: Individual setting-specific minerals sets for reservoir temperature estimation.

| URG | Iceland | El Tatio | Waiotapu | Miravalles | Pannonia | Paris | Molasse |
|---|---|---|---|---|---|---|---|
| Quartz | Quartz | Chalcedony | Quartz | Chalcedony | Quartz | Quartz | Quartz |
| K-feldspar | K-feldspar | K-feldspar | K-feldspar | K-feldspar | K-feldspar | K-feldspar | K-feldspar |
| Microcline | Microcline | Microcline | Microcline | Microcline | Microcline | Microcline | Microcline |
| Albite | Albite | Albite | Albite | Albite | Albite | Albite | Albite |
| Muscovite | Muscovite | Muscovite | Muscovite | Muscovite | Muscovite | Muscovite | Muscovite |
| Illite | Illite | Illite | | Illite | Illite | Illite | Illite |
| Diaspore | Diaspore | Diaspore | Diaspore | Diaspore | Diaspore | Diaspore | Diaspore |
| Analcime | Analcime | Analcime | Analcime | Analcime | Analcime | Analcime | |
| Scolecite | | Scolecite | Scolecite | Scolecite | Scolecite | Scolecite | Scolecite |
| Anhydrite | Anhydrite | Anhydrite | Anhydrite | Anhydrite | | Anhydrite | Anhydrite |
| Kaolinite | | Kaolinite | | Kaolinite | Kaolinite | Kaolinite | Kaolinite |
| Pyrophyllite | | Pyrophyllite | | Pyrophyllite | Pyrophyllite | Pyrophyllite | Pyrophyllite |
| Montmor. | Montmor. | Montmor. | Montmor. | Montmor. | Montmor. | Montmor. | Montmor. |
| Beidellite | | Beidellite | Beidellite | Beidellite | Beidellite | Beidellite | Beidellite |
| | Calcite | | | Calcite | Calcite | Calcite | Calcite |
| | Sanidine | | Sanidine | Sanidine | Sanidine | Sanidine | |
| Smectite | Smectite | | Smectite | | Smectite | | Smectite |
| | | Mesolite | Mesolite | Mesolite | | | Mesolite |
| | | Stiblite | Stiblite | Stiblite | Stiblite | | Stiblite |
| | | | Saponite | Saponite | | Saponite | Saponite |
| Paragonite | | Paragonite | | | Paragonite | Paragonite | |
| Tremolite | Tremolite | | | | | | |
| | Clinochlore | | | | Clinochlore | | Clinochlore |
| Laumontite | Laumontite | | | Laumontite | | | |
| Gibbsite | | | | | Gibbsite | Gibbsite | Gibbsite |
| | | | | | Dolomite | Dolomite | Dolomite |
| | | | Clinoptilolite | | Clinoptilolite | | |
| | Enstatite | | | | Enstatite | | |
| | Wollastonite | | | Wollastonite | | | |
| | Wairakite | | | | | | |

**References**

Arnórsson, S., Björnsson, S., Muna, Z. W., and Bwire-Ojiambo, S., 1990: The use of gas chemistry to evaluate boiling processes and initial steam fractions in geothermal reservoirs with an example from the Olkaria field, Kenya, Geothermics, 19, 497–514, https://doi.org/10.1016/0375-6505(90)90002-S.

ASTM D1141-98, 2013: Standard Practice for the Preparation of Substitute Ocean Water, ASTM International, West Conshohocken, PA, https://doi.org/10.1520/D1141-98R13.

Banwell, C. J., 1959: Waiotapu Geothermal Field - Chapter VIII: Programming of Temperature Surveys, Bulletin, 155.

Bjarnason, J. Ö., 2010: WATCH: The chemical speciation program, ÍSOR – Iceland Geosurvey, Reykjavík, Iceland.

Charlton, S. R. and Parkhurst, D. L., 2011: Modules based on the geochemical model PHREEQC for use in scripting and programming languages, Computers & Geosciences, 37, 1653–1663, https://doi.org/10.1016/j.cageo.2011.02.005.

Cooper, D. C., Palmer, C. D., Smith, R. W., and McLing, T. L., 2013: Multicomponent Equilibrium Models for Testing Geothermometry Approaches, 38th Workshop on Geothermal Reservoir Engineering.

Criaud, A., Fouillac, C., and Marty, B., 1989: Low enthalpy geothermal fluids from the Paris Basin - 2 Oxidation-reduction state and consequences for the prediction of corrosion and sulfide scaling, Geothermics, 18.

Dennis, B. R., Lawton, R. G., Kolar, J. D., and Alvarado, A., 1989: Results of Investigation at the Miravalles Geothermal Field, Costa Rica Part 1: Well Logging: LA-1510-MS, Part 1, Los Alamos National Laboratory.

Dezayes, C., Sanjuan, B., Gal, F., Lerouge, C., and Brach, M., 2013: Forage d'exploration géothermique GRT1: suivi géochimique des fluides et caractérisation des zones fracturées, Rapport final. BRGM/RP - 62546-FR.

Ellis, A. J., 1970: Quantitative interpretation of chemical characteristics of hydrothermal systems, Geothermics, 2, 516–528, https://doi.org/10.1016/0375-6505(70)90050-7.

Ellis, A. J., 1963: The solubility of calcite in sodium chloride solutions at high temperatures, American Journal of Science, 261, 259–267, https://doi.org/10.2475/ajs.261.3.259.

Ellis, A. J. and Mahon, W., 1964: Natural hydrothermal systems and experimental hot-water/rock interactions, Geochimica et Cosmochimica Acta, 28, 1323–1357, https://doi.org/10.1016/0016-7037(64)90132-2.

Ellis, A. J. and Mahon, W. A. J., 1977: Chemistry and geothermal systems, Energy science and engineering Resources, technology, management, Academic Press, New York, 392 pp.

Fournier, R. O. and Rowe, J. J., 1966: Estimation of underground temperatures from the silica content of water from hot springs and wet-steam wells, American Journal of Science, 264, 685–697, https://doi.org/10.2475/ajs.264.9.685.

Fournier, R. O. and Truesdell, A. H., 1974: Geochemical indicators of subsurface temperature - Part 2, Estimation of temperature and fraction of hot water mixed with cold water, Journal of Research of the U.S. Geological Survey, 263–270, https://doi.org/10.3133/ofr741032.

Gherardi, F., Panichi, C., Yock, A., and Gerardo-Abaya, J., 2002: Geochemistry of the surface and deep fluids of the Miravalles volcano geothermal system (Costa Rica), Geothermics, 31, 91–128, https://doi.org/10.1016/S0375-6505(01)00030-X.

Giggenbach, W. F., 1988: Geothermal solute equilibria. Derivation of Na-K-Mg-Ca geoindicators, Geochimica et Cosmochimica Acta, 52, 2749–2765, https://doi.org/10.1016/0016-7037(88)90143-3.

Giggenbach, W. F., 1981: Geothermal mineral equilibria, Geochimica et Cosmochimica Acta, 45, 393–410, https://doi.org/10.1016/0016-7037(81)90248-9.

Giggenbach, W. F., 1978: The isotopic composition of waters from the El Tatio geothermal field, Northern Chile, Geochimica et Cosmochimica Acta, 42, 979–988, https://doi.org/10.1016/0016-7037(78)90287-9.

Giggenbach, W., Sheppard, D. S., Robinson, B. W., Stewart, M. K., and Lyon, G. L., 1994: Geochemical structure and position of the Waiotapu geothermal field, New Zealand, Geothermics, 23, 599–644, https://doi.org/10.1016/0375-6505(94)90022-1.

Guðmundsson, B. T. and Arnórsson, S., 2002: Geochemical monitoring of the Krafla and Námafjall geothermal areas, N-Iceland, Geothermics, 31, 195–243, https://doi.org/10.1016/S0375-6505(01)00022-0.

Langelier, W. F. and Ludwig, H. F., 1942: Graphical Methods for Indicating the Mineral Character of Natural Waters, Journal - American Water Works Association, 34, 335–352, https://doi.org/10.1002/j.1551-8833.1942.tb19682.x.

Marty, B., Criaud, A., and Fouillac, C., 1988: Low enthalpy geothermal fluids from the Paris sedimentary basin - 1 Characteristics and origin of gases, Geothermics, 17, 619–633.

Michard, G. and Bastide, J.-P., 1988: Etude geochimique de la nappe du dogger du bassin parisien, Journal of Volcanology and Geothermal Research, 35, 151–163, https://doi.org/10.1016/0377-0273(88)90012-1.

Nitschke, F., 2018: Numerical and Experimental Characterization of Dissolution and Precipitation Processes in Deep Geothermal Reservoirs, Dissertation, Karlsruhe Institute of Technology (KIT).

Nitschke, F., Held, S., Neumann, T., and Kohl, T., 2018: Geochemical characterization of the Villarrica geothermal system, Southern Chile, part II: Site-specific re-evaluation of SiO2 and Na-K solute geothermometers, Geothermics, 74, 217–225, https://doi.org/10.1016/j.geothermics.2018.03.006.

Nitschke, F., Held, S., Villalon, I., Neumann, T., and Kohl, T., 2017: Assessment of performance and parameter sensitivity of multicomponent geothermometry applied to a medium enthalpy geothermal system, Geotherm Energy, 5, 1, https://doi.org/10.1186/s40517-017-0070-3.

Olguín-Martínez, M.G., Peiffer, L., Dobson, P.F., Spycher, N., Inguaggiato, C., Wanner, C., Hoyos, A., Wurl, J., Makovsky, K., Ruiz-Aguilar, D., 2022: PyGeoT: A tool to automate mineral selection for multicomponent geothermometry Geothermics 104, 102467 (2022). doi: 10.1016/j.geothermics.2022.102467

Óskarsson, F., Fridriksson, T., and Thorbjörnsson, D., 2015: Geochemical Monitoring of the Reykjanes Geothermal Reservoir 2003 to 2013, World Geothermal Congress 2015.

Palmer, C. D., 2014: Reservoir Temperature Estimator (RTEst): User's Manual, p. 10.

Parkhurst, D. L. and Appelo, C. A. J., 2013: Description of Input and Examples for PHREEQC Version 3—A Computer Program for Speciation, Batch-Reaction, One-Dimensional Transport, and Inverse

Geochemical Calculations, U.S. Geological Survey Techniques and Methods, 497 p., available at: https://pubs.usgs.gov/tm/06/a43/.

Peiffer, L., Wanner, C., Spycher, N., Sonnenthal, E. L., Kennedy, B. M., and Iovenitti, J., 2014: Optimized multicomponent vs. classical geothermometry: Insights from modeling studies at the Dixie Valley geothermal area, Geothermics, 51, 154–169, https://doi.org/10.1016/j.geothermics.2013.12.002.

Reed, M. H. and Spycher, N., 1984: Calculation of pH and mineral equilibria in hydrothermal waters with application to geothermometry and studies of boiling and dilution, Geochimica et Cosmochimica Acta, 48, 1479–1492, https://doi.org/10.1016/0016-7037(84)90404-6.

Sanjuan, B., Millot, R., Innocent, C., Dezayes, C., Scheiber, J., and Brach, M., 2016: Major geochemical characteristics of geothermal brines from the Upper Rhine Graben granitic basement with constraints on temperature and circulation, Chemical Geology, 428, 27–47, https://doi.org/10.1016/J.CHEMGEO.2016.02.021.

Sanjuan, B., Jacquot, E., Guigues, N., Foucher, J.-C., Brach, M., and Braibant, G., 2001: Field geochemistry contribution, Annex 2 (BRGM contribution) of the final EEC report (European hot dry rock geothermal research programme April 1998–June 2001), JOR3-CT98-0313.

Schindler, M., Baumgärtner, J., Gandy, T., Hauffe, P., Hettkamp, T., Menzel, H., Penzkofer, P., Teza, D., Tischner, T., and Wahl, G., 2010: Successful Hydraulic Stimulation Techniques for Electric Power Production in the Upper Rhine Graben, Central Europe.

Sonnenthal, N.; Spycher, N.; Peiffer, L. and E., 2013: GeoT User's Guide: A Computer Program for Multicomponent Geothermometry and Geochemical Speciation, Version 1.4, Lawrence Berkeley National Laboratory.

Spycher, N., Peiffer, L., Sonnenthal, E. L., Saldi, G., Reed, M. H., and Kennedy, B. M., 2014: Integrated multicomponent solute geothermometry, Geothermics, 51, 113–123, https://doi.org/10.1016/j.geothermics.2013.10.012.

Spycher, N., Sonnenthal, E. L., and Kennedy, B. M., 2011: Integrating multicomponent chemical geothermometry with parameter estimation computations for geothermal exploration, 35, pp. 663-666.

Varsányi, I., Matray, J.-M., and Ó.Kovács, L., 1997: Geochemistry of formation waters in the Pannonian Basin (southeast Hungary), Chemical Geology, 140, 89–106, https://doi.org/10.1016/S0009-2541(97)00045-4.

Vidal, J. and Genter, A., 2018: Overview of naturally permeable fractured reservoirs in the central and southern Upper Rhine Graben: Insights from geothermal wells, Geothermics, 74, 57–73, https://doi.org/10.1016/j.geothermics.2018.02.003.

Vidal, J., Hehn, R., Glaas, C., and Genter, A., 2019: How Can Temperature Logs Help Identify Permeable Fractures and Define a Conceptual Model of Fluid Circulation? An Example from Deep Geothermal Wells in the Upper Rhine Graben, Geofluids, 2019, 1–14, https://doi.org/10.1155/2019/3978364.

Ystroem, L. H., Nitschke, F., Held, S., and Kohl, T., 2021: An Integrated Sensitivity Analysis for the Basalt Specific Multicomponent Geothermometer for High Temperature Settings, Proceedings World Geothermal Congress 2020+1, Reykjavik, Iceland.

Ystroem, L. H., Nitschke, F., Held, S., and Kohl, T., 2020: A multicomponent geothermometer for high-temperature basalt settings, Geotherm Energy, 8, 13, https://doi.org/10.1186/s40517-020-0158-z.